Nanoscale Advances

ROYAL SOCIETY OF CHEMISTRY

PAPER

View Article Online
View Journal | View Issue

Cite this: *Nanoscale Adv.*, 2020, **2**, 2587

IR820 functionalized melanin nanoplates for dual-modal imaging and photothermal tumor eradication†

Botao Qu, ‡ Xiaomin Zhang,‡ Yahong Han, Xiaoyang Peng, Jinghua Sun and Ruiping Zhang*

Received 26th March 2020
Accepted 4th May 2020

DOI: 10.1039/d0na00236d

rsc.li/nanoscale-advances

Melanin as an endogenous biomolecule is widely applied in the biomedical field, focusing especially on diagnostic imaging and photothermal therapy in cancer treatment. However, its photothermal conversion efficiency, a benchmark in tumor photothermal therapy (PTT), often could not satisfy PTT requirements to some degree, and this greatly influenced its use in photothermal cancer therapy. As for fluorescence imaging, a small-molecule NIR dye as a fluorescence probe is easily and rapidly metabolized *in vivo*, resulting in low accumulation in a tumor. To overcome these problems, we attempt to use melanin as a carrier to conjugate a fluorochrome, a recombinant small NIR dye IR820 nanoplatform containing melanin (MNP-PEG-IR820 abbreviated to MPI). The addition of IR820 not only enhances the PTT ability of the nanoplatform, but also endows the material with excellent NIR fluorescence behavior. Most importantly, the integration of fluorescence dye and melanin improves the circulation and stability performance of IR820 while reducing its toxicity *in vivo*, owing to the protectivity of melanin. Thus, the diagnostic capability is enhanced. Meanwhile, the behavior of the nanoplatform in PAI/PTT is significantly improved. The *in vitro* investigations reveal that the MPI NPs afford a potent PTT effect and ideal resistance to photobleaching. After intravenous injection, the MPI NPs display effective PTT tumor eradication in a Hep-2 tumor bearing mouse model with excellent dual NIR-I fluorescence/photoacoustic imaging guided phototherapy. Hence, our work shows the potential of MPI NPs as nano-theranostics for biomedical application to laryngocarcinoma.

1. Introduction

In the past few years, melanin as an endogenous biomacromolecule has attracted a lot of attention due to its unique physical and chemical properties as well as its promising applications in opto-bioelectronics, nanomedicine, cancer diagnosis and therapy.[1–3] It is well known that melanin is widely distributed in nature as a pigment in hair, skin, and eyes, and is an important component of living organisms. Natural melanin with its macromolecular structure has many fascinating properties, including structural coloration, photoprotection, photosensitization, free-radical scavenging, metal ion chelation and antioxidant activity.[4–6] Structurally, melanin is constituted of 5,6-dihydroxyindole (DHI) units which endow it with strong coordination capacities with metals by diverse modes. Meanwhile, the abundant catechol structures of melanin favor its modification by functional molecules for specific bioapplications. Importantly, melanin can effectively load drugs through π–π stacking interactions.[7] Besides this, melanin shows broadband light absorption spanning across the entire UV-visible-NIR range, which makes it suitable for optoacoustic imaging.[8] This implies that melanin possesses modest photothermal behavior. Form the conditions mentioned above, it is necessary to investigate structure–property relationships in detail, which will guide us to better understand and track the path toward a rational design of next-generation melanin-based functional materials for various biomedical and technological applications.

Photothermal therapy (PTT) as a non-invasive method for cancer therapy has aroused widespread attention over the last decade.[9–14] PTT destroys tumor cells by employing light-absorbing agents to generate localized heat under continuous NIR irradiation. In view of the recognized advantages of PTT, such as minimal invasiveness, noninvasive penetration and low toxicity, PTT has been shown to be a promising strategy to treat cancer. Significantly, PTT is often accompanied by the appearance of photoacoustics.[15–20] Photoacoustic imaging (PAI), which converts optical energy to acoustic waves with PA contrast agents, exhibits considerable merits, such as deep tissue

School of Basic Medical Sciences, Shanxi Medical University, Imaging College of Shanxi Medical University, The Affiliated Bethune Hospital of Shanxi Medical University, Taiyuan 030001, P. R. China. E-mail: zrp_7142@163.com

† Electronic supplementary information (ESI) available. See DOI: 10.1039/d0na00236d

‡ Contributed equally to this work.

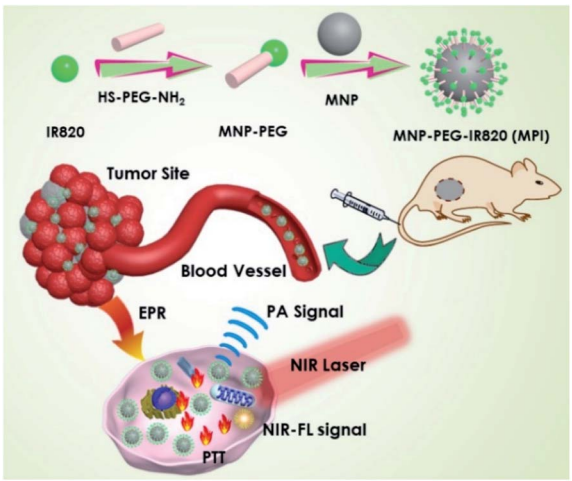

Scheme 1 The preparation process of MNP-PEG-IR820 (MPI) and its application for dual-modal imaging and the photothermal therapy of cancer.

penetration, high spatial resolution, and high signal–noise ratio in comparison with conventional techniques.[21–26] Likewise, NIR imaging with real-time behavior, noninvasiveness and high sensitivity has been developed for disease diagnosis.[27–36] However, its shortcomings, such as shallow tissue penetration depth, low spatial resolution and rapid, limit its clinical application.[37–43] Fortunately, PA imaging perfectly overcomes these problems. The combination of multiple imaging modalities is highly beneficial to locating cancerous tumors and real-time *in vivo* visualization-guided tumor therapy, providing a complementary imaging modality to acquire comprehensive information about a tumor.[44–48]

Herein, we present a simple method to prepare IR820 functionalized MNP (MPI) nanoplates for dual-modal imaging and cancer therapy mediated by laser irradiation in the NIR window. Such MPI shows strong absorbance in the NIR-I bio-window for PA imaging and showed potential for photothermal therapy. MPI NPs have several advantages. First, the functionalization of IR820 dyes endows MPI with an NIR fluorescent property. Second, the PTT performance of MPI is obviously improved, resulting in strong hyperthermal ablation of cancer cells. Third, the integration of fluorescence dye improves IR820 circulation and reduces its toxicity *in vivo*. For this purpose, an exploration of melanin-based phototheranostic agents shows great potential in the field of molecular imaging and antitumor therapy (Scheme 1).

2. Results and discussion

2.1 Preparation and characterization of MPI

Melanin NPs (MNP) were first fabricated by probe sonication in NaOH solution.[49] Transmission electron microscopy (TEM) demonstrated that the MNP were uniform with a diameter of around 4.3 nm (Fig. S1†). MPI nanoplates were synthesized *via* the HS-PEG-NH_2 coupling of IR820 and MNP.[50] The transmission electron microscopy (TEM) image revealed that the size of the MPI

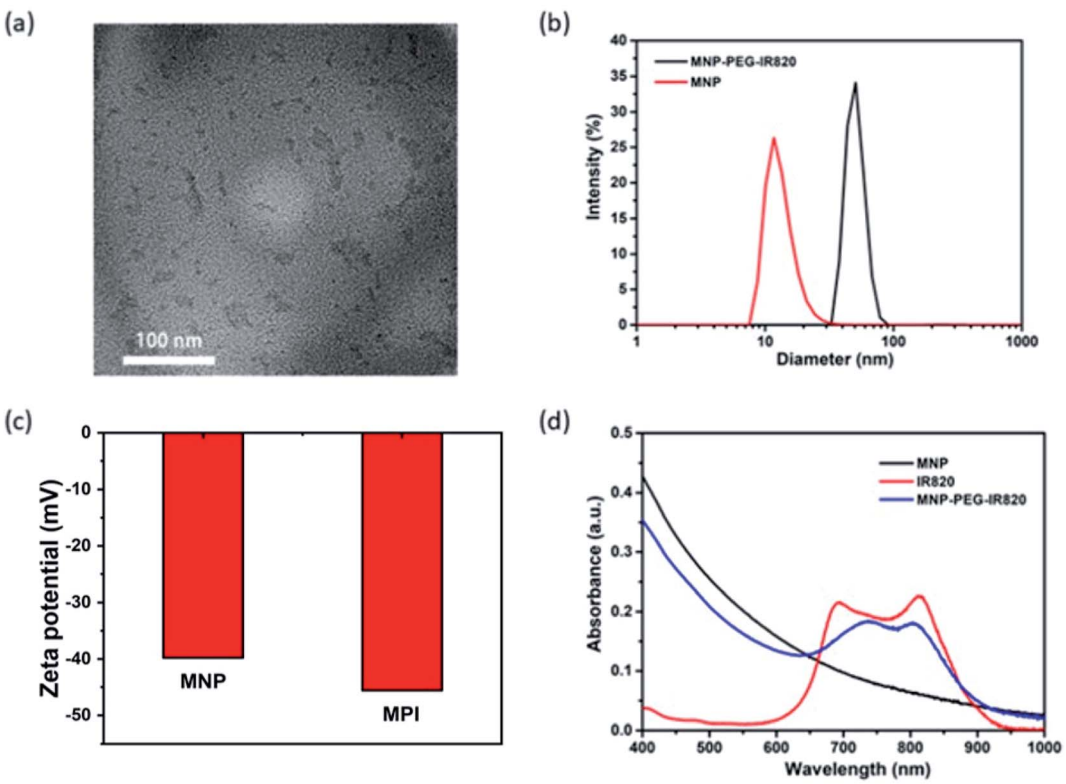

Fig. 1 Characterization of MPI NPs. (a) TEM images of MPI. (b) Hydrodynamic diameters of MNP and MPI. (c) Zeta potential of MNP and MPI at pH 7.4. (d) UV-vis-NIR absorption spectra of MNP, IR820 and MPI in PBS solution.

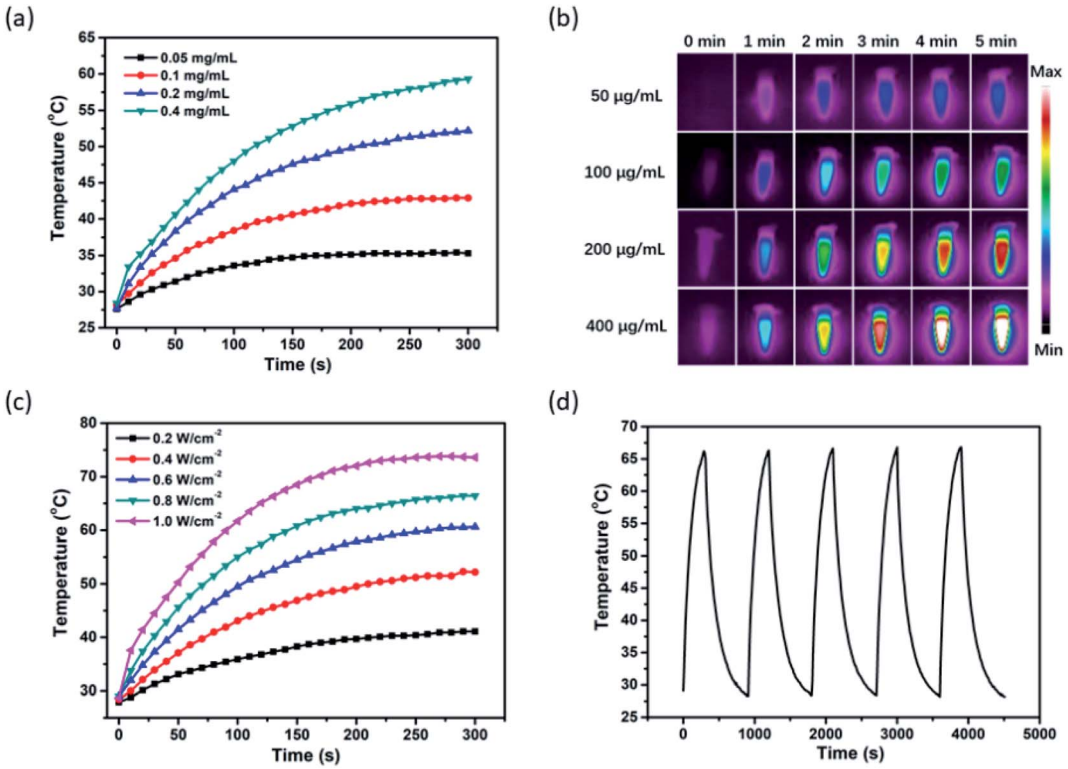

Fig. 2 Photothermal effect of MPI. (a) Photothermal curves and (b) infrared thermal images of MPI at various concentrations under 808 nm laser irradiation at 0.4 W cm^{-2} for 5 min. (c) Temperature change curves of MPI solutions (0.2 mg mL^{-1}) irradiated with an 808 nm laser with different power densities for 5 min. (d) Temperature variation of MPI solution over five cycles of 808 nm NIR laser on/off irradiation.

NPs ranged from 16.3 to 53.6 nm (Fig. 1a), which was smaller than the result obtained from dynamic light scattering (DLS) with an average diameter of 50.7 nm (Fig. 1b). This change in size may be due to the swelling of PEG chains and surface hydration of NPs.[51] Additionally, the zeta potential was determined to be −36.6 mV for MNP and −45.6 mV for MPI, verifying the successful conjugation of IR820 (Fig. 1c). Fourier-transform infrared (FT-IR) analysis was applied to characterize the products (Fig. S2†). IR820-PEG showed characteristic absorption peaks of PEG at 2884 cm^{-1} (alkyl C–H stretching) and 1112 cm^{-1} (C–O–C stretching),[52] confirming the grafting of PEG onto the surface of IR820. The presence of the sharp absorption peak at 1381 cm^{-1} for the C–H vibrations in the spectra of MPI demonstrated the modification of MNP (Fig. 1d). The fluorescence spectra (FL) of MPI were further studied (Fig. S3†). The maximum emission peak was observed centered at 830 nm, implying its potential application for *in vivo* NIR-FL imaging. In addition, UV-vis spectroscopy further confirmed the successful fabrication of MPI (Fig. 1e), in accordance with the results of FT-IR and DLS analysis. After functionalizing MNP with IR820, MPI showed a wide absorption range from 400 to 1000 nm (Fig. 1d), showing strong NIR bio-window behavior that makes it eligible for dual-modal imaging-guided PTT therapy.

2.2 Photothermal properties of MPI

In light of the considerable NIR-I bio-window absorption of MPI, which makes MPI suitable to be a PTT agent for cancer therapy, the PTT properties of MPI were investigated under 808 nm laser irradiation. As expected, the MPI solution displayed an obvious concentration-dependent temperature enhancement. As shown in Fig. 2a, with the rise in MPI concentration from 0.05 to 0.4 mg mL^{-1}, the temperature increased by 35.3 °C, 42.9, 52.2, and 59.3 °C, respectively. Moreover, the PTT images of different concentrations of MPI solutions were observed by infrared thermal imaging (Fig. 2b). For example, when MPI solution (0.2 mg mL^{-1}) was irradiated with an NIR laser (808 nm, 0.4 W cm^{-2}), the temperature increased from 28.2 to 52.2 °C after 5 min of laser irradiation, accompanied by a color change of the PTT images from purple to red. The photothermal conversion efficiency (η) of MPI is determined to be 24.7%, superior to that of MNP-Mn (18%), as reported by our group (Fig. S4 and S5†).[8] The relationship between power density and temperature was investigated in turn. The temperature of MPI solution (0.2 mg mL^{-1}) increased sharply with a rise in power density upon 808 nm laser irradiation within 5 min, confirming the linear dependency between temperature and laser power density (Fig. 2c). When MPI was irradiated with an 808 nm laser for five on–off cycles, no significant decrease in temperature was observed, implying the superior PTT stability of such MPI NPs (Fig. 2d). Taken together, MPI NPs exhibit excellent PTT behavior and hold great potential for NIR-mediated PTT tumor ablation.

2.3 *In vitro* NIR-I fluorescence and photoacoustic properties of MPI

In light of the outstanding optical properties of MPI, its NIR-I fluorescence was investigated *in vitro*. As shown in Fig. 3a,

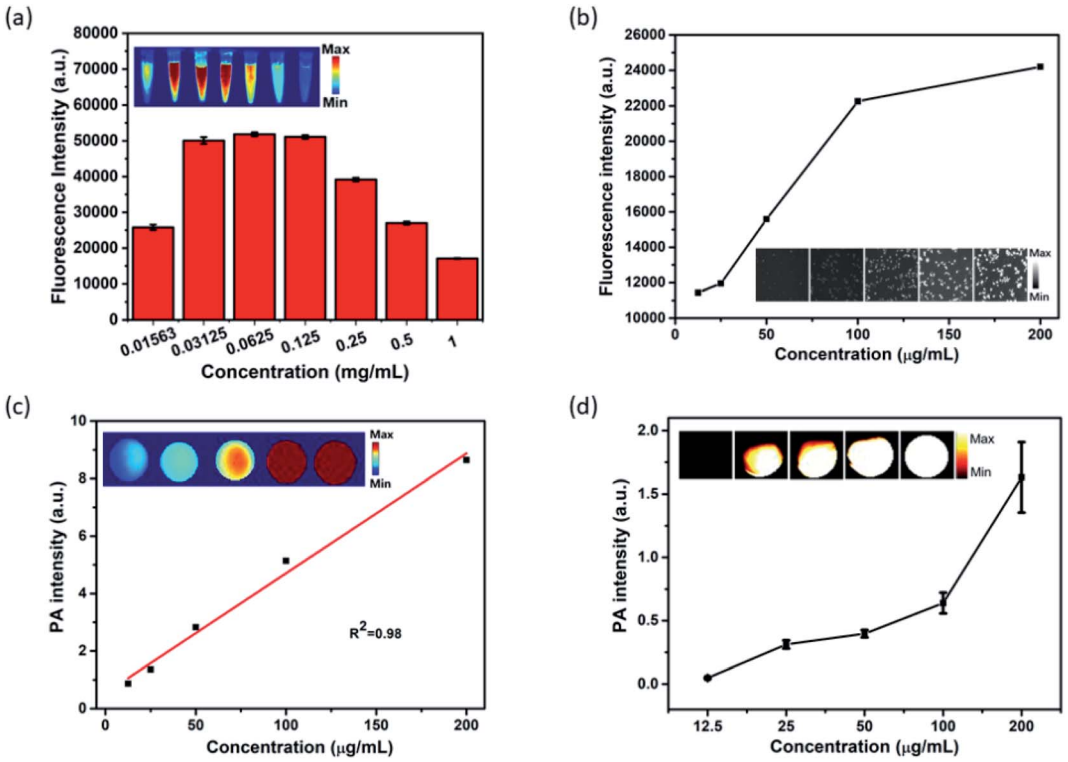

Fig. 3 *In vitro* NIR-I fluorescence and photoacoustic properties of MPI. (a) Fluorescence imaging of MPI at different concentrations. (b) NIR-I fluorescence imaging of Hep-2 cells incubated with MPI at various concentrations. (c) Photoacoustic imaging of MPI at different concentrations. (d) Photoacoustic imaging of Hep-2 cells incubated with MPI at different concentrations.

there are two stages in the FL signal with variation in concentration. Foremost, when the concentration of MPI increased from 0.01563 to 0.0625 mg mL^{-1}, the FL signal intensity increased rapidly, then the FL signal intensity decreased gradually with increasing concentration ranging from 0.0625 to 1 mg mL^{-1}. This phenomenon may be ascribed to the fluorescence self-quenching effect due to the self-aggregation of IR820 at high concentrations.[53] Subsequently, fluorescence imaging at the cellular level was discussed. The FL intensity of Hep-2 cells incubated with MPI was found to increase with increasing concentration, due to the cellular uptake of nanoplates by Hep-2 cells. The gradually brightening NIR-I images clearly showed that MPI is suitable for serving as an NIR-I fluorescence contrast agent (Fig. 3b). Encouraged by the excellent NIR absorption and PTT properties of MPI, the PA property of MPI was evaluated *in vitro*. As illustrated in Fig. 3a, the intensity of the PA signal and brightness of the PA images are proportional to the MPI concentration ranging from 0.0125 to 0.2 mg mL^{-1}, showing a linear correlation with $R^2 = 0.98$. Subsequently, the outcome from a PA imaging assay in Hep-2 cells was analogous to the above-mentioned results (Fig. 3b). These results indicated that the MPI is an efficient NIR-I fluorescence/PA dual-modal imaging probe.

2.4 *In vitro* cellular uptake and cytotoxicity of MPI

Cellular uptake of MPI was investigated by confocal laser scanning microscopy (CLSM) and flow cytometry. According to the CLSM images, bright green fluorescence was clearly observed in Hep-2 cells after 4 h of incubation (Fig. 4a), which was in accordance with the FL imaging and PA imaging of Hep-2 cells. The observations obtained from flow cytometry analysis agree well with the CLSM results. Meanwhile, flow cytometry analysis further proved that the internalization of MPI achieved near saturation after 4 h as the incubation time increased from 0 to 6 h, confirming that MPI was localized inside the cells in a time-dependent manner (Fig. 4b). Before application in PTT, the *in vitro* cytotoxicity of MPI toward Hep-2 cells was evaluated using a Cell Counting Kit-8 (CCK-8) assay (Fig. 4c). The results illustrated that MPI has no evident toxic effects on Hep-2 cells even at a high concentration of up to 100 μg mL^{-1} within 24 h, implying the outstanding biocompatibility of MPI. Subsequently, cell viability was evaluated by a live/dead assay, where cells labeled with calcein-AM and PI emit green and red fluorescence, respectively. In Fig. 4d, the group treated by laser and the groups treated with PBS or MPI without NIR irradiation exhibit vivid green fluorescence, demonstrating negligible cell damage. However, the group of Hep-2 cells treated with MPI under excitation at 808 nm exhibited widespread red fluorescence, suggesting that MPI could effectively destroy cancer cells by NIR laser irradiation. Subsequently, apoptosis and necrosis analysis of the cells were investigated by flow cytometry. As shown in Fig. 4e, the results of flow cytometry analysis were consistent with the live/dead cell staining assay. Without NIR irradiation, cells show a high survival ratio and negligible

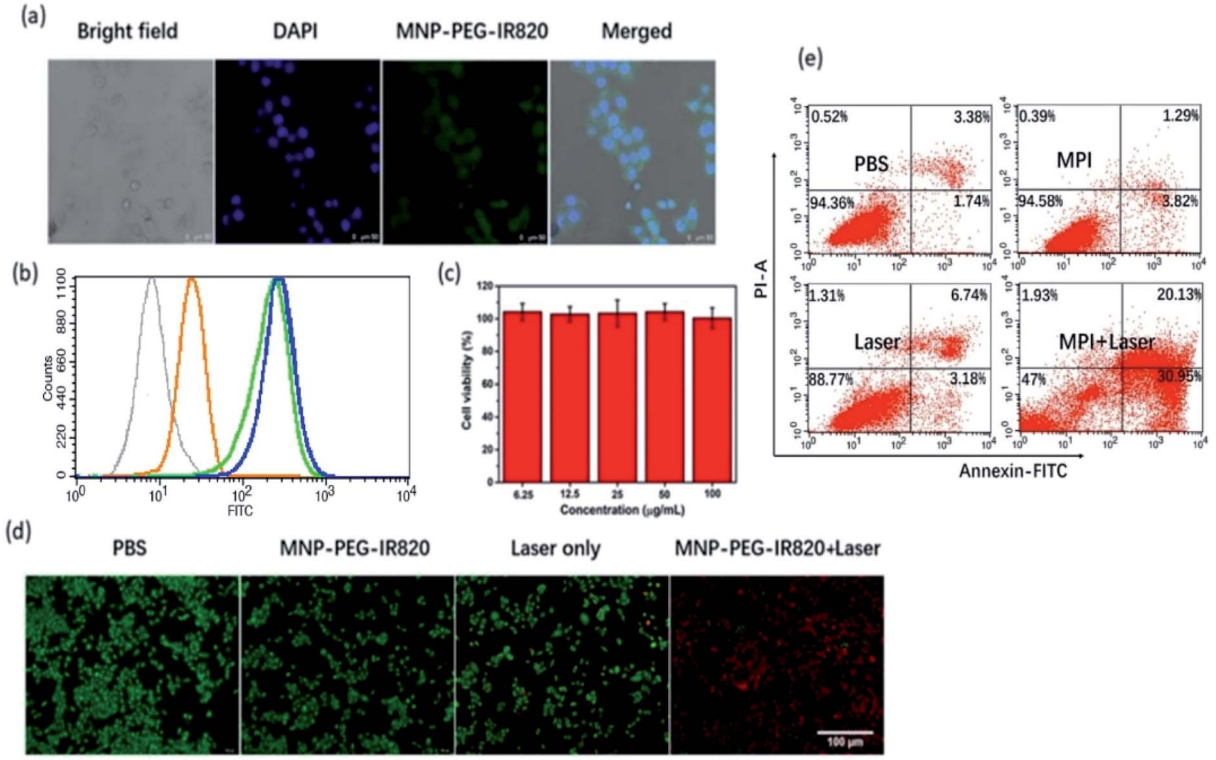

Fig. 4 The cellular uptake and cytotoxicity of MPI. (a) CLSM images of Hep-2 cells incubated with MPI for 4 h (scale bar: 50 μm). (b) Flow cytometry analysis of Hep-2 cells treated with MPI after incubation for 0 h (gray curve), 2 h (yellow curve), 4 h (green curve) and 6 h (blue curve). (c) Cell viability of Hep-2 cells treated with different concentrations of MPI without laser irradiation. (d) Live/dead assays and (e) cell apoptosis assay of Hep-2 cells treated with MPI with or without laser irradiation (scale bars: 100 μm).

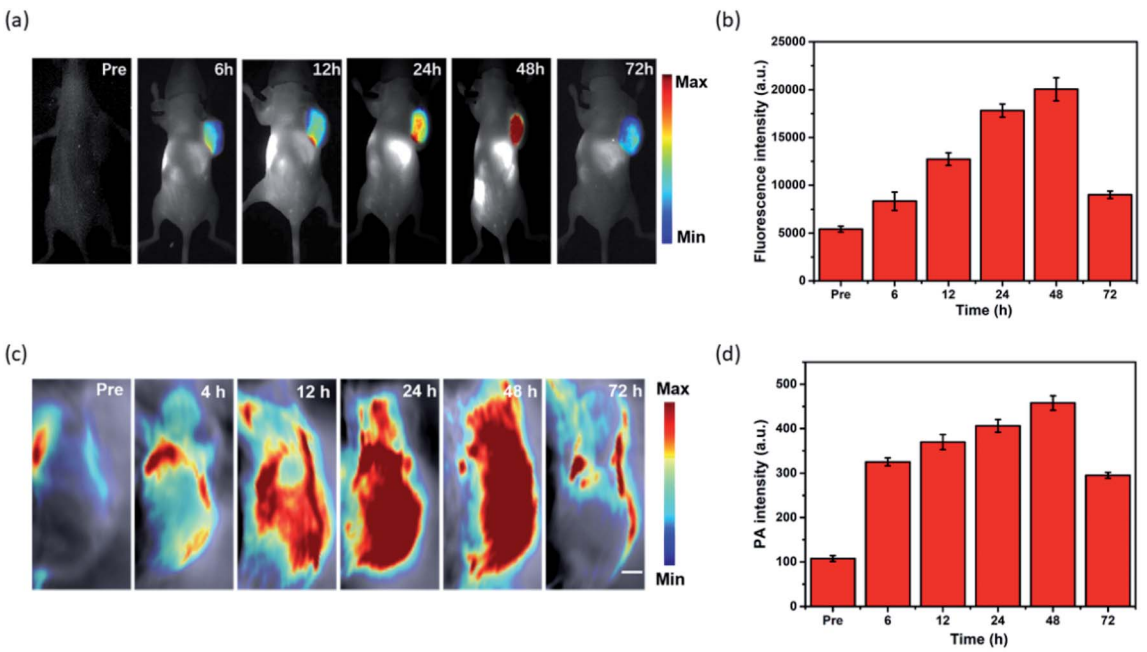

Fig. 5 NIR-I fluorescence imaging and photoacoustic imaging of tumor site *in vivo*. (a) NIR-I fluorescence imaging and (b) signal intensity changes of tumor site of Hep-2 tumor-bearing mice taken at 6, 12, 24, 48 and 72 h after intravenous administration of MPI. (c) Photoacoustic imaging and (d) signal intensity changes of tumor site of Hep-2 tumor-bearing mice after i.v injection with MPI (scale bars: 1.0 mm).

apoptosis or dead behavior. Once treated with NIR irradiation, apparently dead cells appeared in the MPI group. These results indicated that MPI could be used as an excellent PTT agent for cancer therapy.

2.5 *In vivo* NIR-I fluorescence imaging and PA imaging

To evaluate the capability of MPI for cancer imaging, *in vivo* dual-modal imaging was investigated in Hep-2 tumor-bearing mice model by tail vein injection of MPI. The NIR fluorescence signal of MPI was monitored at various time points. As shown in Fig. 5a and b, the FL signal was gradually enhanced in the tumor region and reached a maximum at 48 h postinjection, implying the tumor accumulation capacity of MPI by an enhanced permeability and retention (EPR) effect.[41–43] Subsequently, the FL signals began to decline due to metabolism. The *in vivo* PA imaging performance was also evaluated in Hep-2 tumor-bearing mice (Fig. 5c and d). The change in PA signal was consistent with that obtained by FL results. The PA signals showed tumor uptake over time and reached maximal retention at 48 h postinjection compared with the signal before injection. As time went on, the PA signal at the tumor site gradually disappeared at 72 h. Therefore, MPI should be a promising dual-modal contrast agent for tumor diagnosis.

2.6 *In vivo* photothermal tumor eradication

To detect the PTT effect of MPI, IR thermal imaging of MPI *in vivo* was first investigated with an 808 nm laser (0.4 W cm^{-2}) for 5 min irradiation 48 h postinjection (Fig. 6a and b). In the group treated with MPI, the temperature of the tumor region rapidly reached 67.9 °C within 5 min, while minimal temperature elevation of the tumor was observed under irradiation for the PBS group. In contrast, the control groups of MPI and PBS without NIR irradiation exhibited negligible temperature change. These results indicated that MPI could effectively absorb NIR energy to produce hyperthermia for photothermal therapy of cancer. Motivated by the excellent performance of MPI demonstrated in the above studies, the antitumor effectiveness was accessed *in vivo* after the tumor volumes had reached about 100 mm^3. Mice with Hep-2 tumor models were divided into four groups (I. PBS; II. Laser; III. MPI; IV. MPI + Laser). As depicted in Fig. 6c–e, the PBS, Laser and MPI groups displayed similar tumor growth, demonstrating that Laser and MPI alone have no influence on the suppression of tumor growth. In comparison, MPI + Laser presents efficient PTT tumor eradication without detectable residual black scars (Fig. S6†). The efficient tumor suppression of MPI may be attributed to the synergetic PTT effect of MNP and IR820. In addition, no apparent variation in body weight was observed for any of the groups, indicating the negligible side effects of MPI *in vivo* (Fig. 6f). We further examined the safety of the material *in vivo* by H&E staining (Fig. S7†). In slices of major organs, including the heart, liver, spleen, lung, and kidney, hardly any apparent injury (including inflammation, cell necrosis and apoptosis) induced by different treatments could be detected. These results confirm that MPI has low toxicity and could be used for *in vivo* PTT therapy.

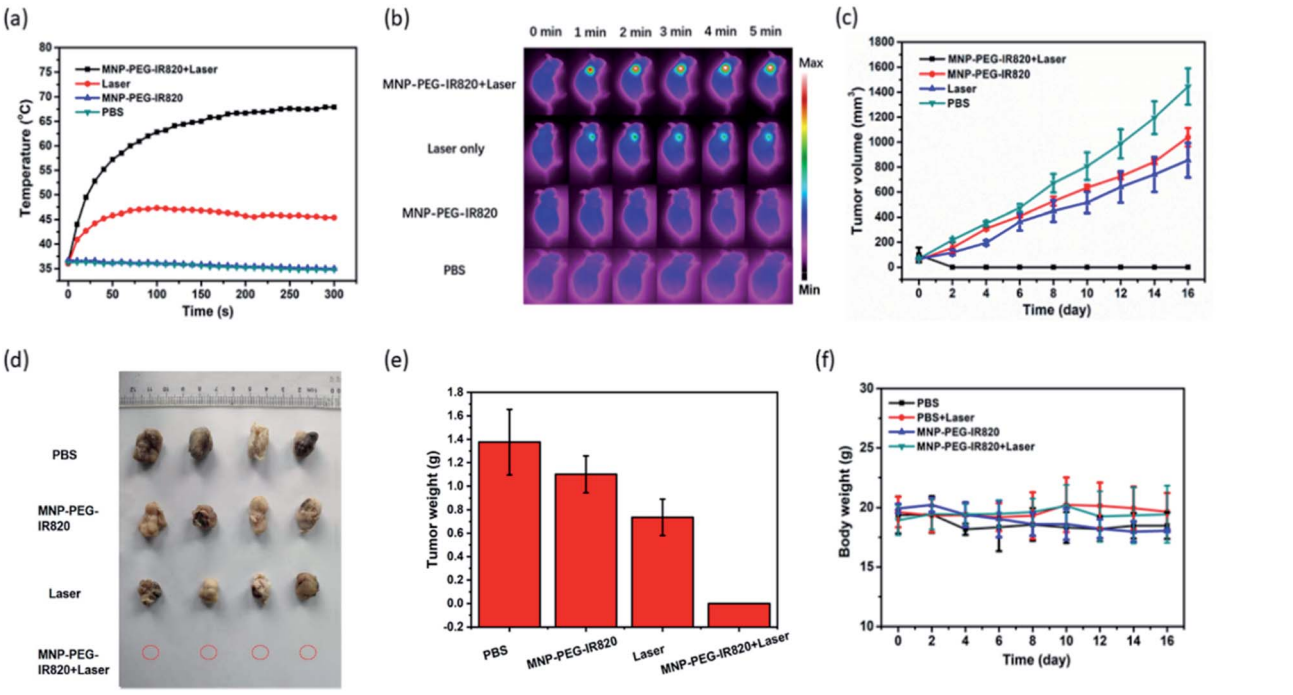

Fig. 6 *In vivo* photothermal therapy. (a) Photothermal curves and (b) IR thermal images of Hep-2 tumor-bearing mice in PBS, MPI, Laser and MPI + Laser groups under 808 nm laser irradiation. (c) Tumor volume growth curve of mice after different treatments (*$p < 0.05$; **$p < 0.01$). (d) Representative photographs of tumors and (e) tumor weight after 16 days of therapy (I. PBS; II. Laser; III. MPI; IV. MPI + Laser). (f) Body weight curves of different groups of mice.

3. Conclusion

In summary, biocompatible MPI NPs were constructed for *in vivo* dual-modal NIR-I fluorescence/photoacoustic Imaging and photothermal eradication of tumors. The resulting small-molecule IR820 dye could not only act as an NIR-I fluorescence agent but also enhanced the PTT performance of melanin. The combination of fluorescence dye and melanin improved the circulation and stability performance of IR820 while reducing toxicity *in vivo*. Meanwhile, the diagnostic capability was enhanced. The fluorescence/PA imaging at the cellular level fully confirmed the internalization of MPI. *In vivo* experiments demonstrated that MPI was effectively accumulated at the tumor site by passive targeting (EPR effect). After the injection of MPI by single-dose intravenous administration, excellent NIR-I fluorescence and photoacoustic imaging were observed in the tumor region, while the performance of enhanced PTT was observed under NIR laser irradiation. More importantly, tumor eradication was achieved after PTT therapy. Thus, melanin-based nanomaterials have great potential for cancer therapy in biological and clinic applications.

Experimental details

The animal procedures were performed in accordance with the Guidelines for Care and Use of Laboratory Animals of Shanxi Medical University, and the experiments were approved by the Animal Ethics Committee of Shanxi Medical University.

Conflicts of interest

There are no conflicts to declare.

Acknowledgements

B. T. Qu and X. M. Zhang contributed equally to this work. This work was financially supported by the National Natural Science Foundation of China (No. 81571747, 81771907), the Science and Technology Innovation Team Project of Shanxi Province (No. 201705D131026), Engineering Technology Research Center of Shanxi Province (No. 201805D121008) Scientific and Technological Achievements Transformation Project of Shanxi Province (No. 201704D131006), the Laboratory Construction Project of Shanxi Province, The Projects for Local Science and Technology Development Guided by the Central Committee (YDZX20191400002537), the Natural Science Foundation of Shanxi Province (No. 201901D111213) and the Startup Foundation for Doctors of Shanxi Medical University (No. 03201505).

References

1 M. d'Ischia, A. Napolitano, A. Pezzella, P. Meredith and M. J. Buehler, *Angew. Chem.*, 2020, DOI: 10.1002/anie.201914276.
2 H. Liu, Y. Yang, Y. Liu, J. Pan, J. Wang, F. Man, W. Zhang and G. Liu, *Adv. Sci.*, 2020, 7, 1903129.
3 M. Caldas, A. C. Santos, F. Veiga, R. Rebelo, R. L. Reis and V. M. Correlo, *Acta Biomater.*, 2020, **105**, 26–43.
4 C. Qi, L.-H. Fu, H. Xu, T.-F. Wang, J. Lin and P. Huang, *Sci. China: Chem.*, 2019, **62**, 162–188.
5 D. L. Longo, R. Stefania, S. Aime and A. Oraevsky, *Int. J. Mol. Sci.*, 2017, **18**, 1719.
6 Y. Liu, K. Ai, X. Ji, D. Askhatova, R. Du, L. Lu and J. Shi, *J. Am. Chem. Soc.*, 2017, **139**, 856–862.
7 R. Zhang, Q. Fan, M. Yang, K. Cheng, X. Lu, L. Zhang, W. Huang and Z. Cheng, *Adv. Mater.*, 2015, **27**, 5063–5069.
8 J. Sun, W. Xu, L. Li, B. Fan, X. Peng, B. Qu, L. Wang, T. Li, S. Li and R. Zhang, *Nanoscale*, 2018, **10**, 10584–10595.
9 C. Song, Y. Li, T. Li, Y. Yang, Z. Huang, J. M. de la Fuente, J. Ni and D. Cui, *Adv. Funct. Mater.*, 2020, **30**, 1906309.
10 B. Li, H. Xiao, M. Cai, X. Li, X. Xu, S. Wang, S. Huang, Y. Wang, D. Cheng, P. Pang, H. Shan and X. Shuai, *Adv. Funct. Mater.*, 2020, **30**, 1909117.
11 S. Zhang, Q. Li, N. Yang, Y. Shi, W. Ge, W. Wang, W. Huang, X. Song and X. Dong, *Adv. Funct. Mater.*, 2019, **29**, 1906805.
12 J. Ouyang, C. Feng, X. Ji, L. Li, H. K. Gutti, N. Y. Kim, D. Artzi, A. Xie, N. Kong, Y. N. Liu, G. J. Tearney, X. Sui, W. Tao and O. C. Farokhzad, *Angew. Chem.*, 2019, **58**, 13405–13410.
13 G. Gao, Y. W. Jiang, H. R. Jia, W. Sun, Y. Guo, X. W. Yu, X. Liu and F. G. Wu, *Biomaterials*, 2019, **223**, 119443.
14 P. Zhang, Y. Hou, J. Zeng, Y. Li, Z. Wang, R. Zhu, T. Ma and M. Gao, *Angew. Chem., Int. Ed.*, 2019, **58**, 11088–11096.
15 Q. Tian, Y. Li, S. Jiang, L. An, J. Lin, H. Wu, P. Huang and S. Yang, *Small*, 2019, **15**, 1902926.
16 Y. Liu, W. Zhen, Y. Wang, J. Liu, L. Jin, T. Zhang, S. Zhang, Y. Zhao, N. Yin, R. Niu, S. Song, L. Zhang and H. Zhang, *Nano Lett.*, 2019, **19**, 5093–5101.
17 R. Zhang, Y. Xu, Y. Zhang, H. S. Kim, A. Sharma, J. Gao, G. Yang, J. S. Kim and Y. Sun, *Chem. Sci.*, 2019, **10**, 8348–8353.
18 Z. Xie, S. Chen, Y. Duo, Y. Zhu, T. Fan, Q. Zou, M. Qu, Z. Lin, J. Zhao, Y. Li, L. Liu, S. Bao, H. Chen, D. Fan and H. Zhang, *ACS Appl. Mater. Interfaces*, 2019, **11**, 22129–22140.
19 S. Liang, X. Deng, Y. Chang, C. Sun, S. Shao, Z. Xie, X. Xiao, P. Ma, H. Zhang, Z. Cheng and J. Lin, *Nano Lett.*, 2019, **19**, 4134–4145.
20 H. Zhang, W. Zeng, C. Pan, L. Feng, M. Ou, X. Zeng, X. Liang, M. Wu, X. Ji and L. Mei, *Adv. Funct. Mater.*, 2019, **29**, 1903791.
21 W. Huang, R. Chen, Y. Peng, F. Duan, Y. Huang, W. Guo, X. Chen and L. Nie, *ACS Nano*, 2019, **13**, 9561–9570.
22 L. Teng, G. Song, Y. Liu, X. Han, Z. Li, Y. Wang, S. Huan, X. B. Zhang and W. Tan, *J. Am. Chem. Soc.*, 2019, **141**, 13572–13581.
23 H. Xiang, H. Lin, L. Yu and Y. Chen, *ACS Nano*, 2019, **13**, 2223–2235.
24 X. Yao, P. Yang, Z. Jin, Q. Jiang, R. Guo, R. Xie, Q. He and W. Yang, *Biomaterials*, 2019, **197**, 268–283.
25 Y. Wang, Z. Sun, Z. Chen, Y. Wu, Y. Gu, S. Lin and Y. Wang, *Anal. Chem.*, 2019, **91**, 2128–2134.
26 Y. Cheng, F. Yang, G. Xiang, K. Zhang, Y. Cao, D. Wang, H. Dong and X. Zhang, *Nano Lett.*, 2019, **19**, 1179–1189.

27 T. Li, C. Li, Z. Ruan, P. Xu, X. Yang, P. Yuan, Q. Wang and L. Yan, *ACS Nano*, 2019, **13**, 3691–3702.
28 S. Wang, Y. Fan, D. Li, C. Sun, Z. Lei, L. Lu, T. Wang and F. Zhang, *Nat. Commun.*, 2019, **10**, 1058.
29 S. He, C. Xie, Y. Jiang and K. Pu, *Adv. Mater.*, 2019, **31**, 1902672.
30 H. Chen, J. Wang, X. Feng, M. Zhu, S. Hoffmann, A. Hsu, K. Qian, D. Huang, F. Zhao, W. Liu, H. Zhang and Z. Cheng, *Chem. Sci.*, 2019, **10**, 7946–7951.
31 M. Duan, F. Xia, T. Li, J. G. Shapter, S. Yang, Y. Li, G. Gao and D. Cui, *Nanoscale*, 2019, **11**, 18426–18435.
32 C. Li, W. Li, H. Liu, Y. Zhang, G. Chen, Z. Li and Q. Wang, *Angew. Chem.*, 2020, **59**, 247–252.
33 X. Song, S. Li, H. Guo, W. You, X. Shang, R. Li, D. Tu, W. Zheng, Z. Chen, H. Yang and X. Chen, *Angew. Chem.*, 2019, **58**, 18981–18986.
34 X. Zeng, L. Xue, D. Chen, S. Li, J. Nong, B. Wang, L. Tang, Q. Li, Y. Li, Z. Deng, X. Hong, M. Wu and Y. Xiao, *Chem. Commun.*, 2019, **55**, 14287–14290.
35 Y. Li, P. Zhang, H. Ning, J. Zeng, Y. Hou, L. Jing, C. Liu and M. Gao, *Small*, 2019, **15**, 1905344.
36 T. Ma, Y. Hou, J. Zeng, C. Liu, P. Zhang, L. Jing, D. Shangguan and M. Gao, *J. Am. Chem. Soc.*, 2018, **140**, 211–218.
37 G. Hong, A. L. Antaris and H. Dai, *Nat. Biomed. Eng.*, 2017, **1**, 0010.
38 J. Cao, B. Zhu, K. Zheng, S. He, L. Meng, J. Song and H. Yang, *Frontiers in Bioengineering and Biotechnology*, 2019, **7**, 487.
39 J. Zhao, D. Zhong and S. Zhou, *J. Mater. Chem. B*, 2018, **6**, 349–365.
40 N. S. James, Y. Chen, P. Joshi, T. Y. Ohulchanskyy, M. Ethirajan, M. Henary, L. Strekowsk and R. K. Pandey, *Theranostics*, 2013, **3**, 692–702.
41 Q. Meng, M. Yu, B. Gu, J. Li, Y. Liu, C. Zhan, C. Xie, J. Zhou and W. Lu, *J. Drug Targeting*, 2010, **18**, 438–446.
42 D. Reichel, M. Tripathi, P. Butte, R. Saouaf and J. M. Perez, *Nanotheranostics*, 2019, **3**, 196–211.
43 A. Fernandez-Fernandez, R. Manchanda, D. A. Carvajal, T. Lei, S. Srinivasan and A. J. McGoron, *Int. J. Nanomed.*, 2014, **9**, 4631–4648.
44 B. Du, C. Qu, K. Qian, Y. Ren, Y. Li, X. Cui, S. He, Y. Wu, T. Ko, R. Liu, X. Li, Y. Li and Z. Cheng, *Adv. Opt. Mater.*, 2019, **8**, 1901471.
45 Y. Sun, F. Ding, Z. Chen, R. Zhang, C. Li, Y. Xu, Y. Zhang, R. Ni, X. Li, G. Yang, Y. Sun and P. J. Stang, *Proc. Natl. Acad. Sci. U. S. A.*, 2019, **116**, 16729–16735.
46 C. Zhang, J. Liu, H. Guo, W. Wang, M. Xu, Y. Tan, T. Huang, Z. Cao, X. Shuai and X. Xie, *Adv. Healthcare Mater.*, 2019, **8**, 1900409.
47 Q. Lin, D. Deng, X. Song, B. Dai, X. Yang, Q. Luo and Z. Zhang, *ACS Nano*, 2019, **13**, 1526–1537.
48 H. B. Cheng, Y. Li, B. Z. Tang and J. Yoon, *Chem. Soc. Rev.*, 2020, **49**, 21–31.
49 Q. Fan, K. Cheng, X. Hu, X. Ma, R. Zhang, M. Yang, X. Lu, L. Xing, W. Huang, S. S. Gambhir and Z. Cheng, *J. Am. Chem. Soc.*, 2014, **136**, 15185–15194.
50 Y. Tang, Y. Li, X. Hu, H. Zhao, Y. Ji, L. Chen, W. Hu, W. Zhang, X. Li, X. Lu, W. Huang and Q. Fan, *Adv. Mater.*, 2018, **30**, 1801140.
51 R. Zhang, C. Qiao, Q. Jia, Y. Wang, H. Huang, W. Chang, H. Wang, H. Zhang and Z. Wang, *Adv. Healthcare Mater.*, 2019, **8**, 1900761.
52 Z. Luo, L. Jiang, S. Yang, Z. Li, W. M. W. Soh, L. Zheng, X. J. Loh and Y. L. Wu, *Adv. Healthcare Mater.*, 2019, **8**, 1900406.
53 B. Wu, B. Wan, S. T. Lu, K. Deng, X. Q. Li, B. L. Wu, Y. S. Li, R. F. Liao, S. W. Huang and H. B. Xu, *Int. J. Nanomed.*, 2017, **12**, 4467–4478.

